



Article

# Fabrication of ZnO-Fe-MXene Based Nanocomposites for Efficient CO<sub>2</sub> Reduction

Karthik Kannan <sup>1</sup>, Mostafa H. Sliem <sup>1</sup>, Aboubakr M. Abdullah <sup>1</sup> ,  
Kishor Kumar Sadasivuni <sup>1,\*</sup>  and Bijandra Kumar <sup>2</sup>

<sup>1</sup> Center for Advanced Materials, Qatar University, P.O. Box, Doha 2713, Qatar; karthik.kannan@qu.edu.qa (K.K.); mostafa@qu.edu.qa (M.H.S.); bakr@qu.edu.qa (A.M.A.)

<sup>2</sup> Department of Technology, Elizabeth City State University, Elizabeth City, NC 27909, USA; bkumar@ecu.edu

\* Correspondence: kishorkumars@qu.edu.qa; Tel.: +974-5058-0237

Received: 13 April 2020; Accepted: 12 May 2020; Published: 15 May 2020



**Abstract:** A ZnO-Fe-MXene nanocomposite was fabricated and examined with diverse spectroscopic techniques. The hexagonal structure of ZnO, MXene, and ZnO-Fe-MXene nanocomposites were validated through XRD. FTIR showed the characteristic vibrational frequencies of ZnO and MXene. The micrographs of the SEM showed nanoparticles with a flower-like structure. The electrocatalytic reduction efficiency of ZnO-Fe-MXene nanocomposite was analyzed through cyclic voltammetry and electrochemical impedance spectroscopy methods. The ZnO-Fe-MXene electrode was confirmed to have a high current density of 18.75 mA/cm<sup>2</sup> under a CO<sub>2</sub> atmosphere. Nyquist plots also illustrated a decrease in the impedance of the ZnO-Fe-MXene layer, indicating fast charge transfer between the Zn and MXene layers. Additionally, this electrochemical study highlights new features of ZnO-Fe-MXene for CO<sub>2</sub> reduction.

**Keywords:** nanocomposites; hydrothermal method; SEM with EDAX; CO<sub>2</sub> reduction

## 1. Introduction

The fundamental problem regarding the conventional burning of fuels is the higher over-potential needed for the conversion of CO<sub>2</sub>. Sustainability and mitigation of the potential contribution to climate change are two key factors that can be gained from the carbon-neutral process of electrochemical carbon dioxide (CO<sub>2</sub>) reduction to fuels. The products from CO<sub>2</sub> electrochemical reduction reactions such as methanol (15.6 MJ/L) and ethanol (24 MJ/L) have energy densities much higher than those of the most advanced battery technologies, making them ideal prototypes for the storage of intermittent renewable energy. Hence, it is an extremely enviable goal to change CO<sub>2</sub> into fuel precursors such as methanol, ethylene, CO, or formic acid using renewable sources of energy (i.e., solar, geothermal, wind, etc.) as the energy input for the process, thereby presenting a convenient way to recycle CO<sub>2</sub> into fuels. The stability and poor product selectivity of the catalysts are some of the problems associated with it. Thus, multi-dimensional approaches have been employed to design new catalysts by synthesizing two-dimensional (2D) materials [1–9].

In modern years, a new variety of 2D material, i.e., MXene, has garnered more attention due to its good electronic conductivity, good chemical stability, and abundant active catalytic sites. Recently, a few studies have shown the potential application of MXenes in electrochemical CO<sub>2</sub> reduction to fuels. Diverse metal oxide nanoparticles, such as CuO, TiO<sub>2</sub>, CdO, MgO, ZnO, and WO<sub>3</sub>, etc., have been suggested for notable applications in carbon dioxide fuel-cell conversion. Compared to the others, zinc oxide has (ZnO, n-type semiconductor, optical bandgap: 3.37 eV) [10] high optical transmittance and low electrical resistivity. ZnO and Fe can be used in the fields of gas sensors, optoelectronics, photovoltaic cells, and fuel cells [11,12].

Considering these properties and its high conductivity and ionic nature in the visible region, it could have wide applications in CO<sub>2</sub> to fuel conversion and methanol sensors, etc. The morphology and structure of materials mainly depend upon the synthesis conditions and opted parameters. To date, several techniques have been used for the synthesis of ZnO nanostructures, such as non-aqueous sol-gel [13], chemical bath deposition [14], combustion [15], co-precipitation [16], electrodeposition [17], microwave-assisted synthesis [18], and microwave-assisted chemical bath deposition [19]. Among these, the hydrothermal method has eminent advantages including high sample purity, low cost, and easy fabrication. Additionally, it has further benefits such as providing a superior surface area, having a controllable particle size, being a low temperature method, creating particles with a narrow particle size distribution, and having a high purity, but it also needs more resources compared to physical methods like melt mixing, laser ablation, electric arc deposition, chemical bath deposition, and ion implantation, etc. ZnO and Fe have electrochemical properties, and the catalytic activity of MXene is good. Previous studies have investigated the synthesis of nanocomposites containing MXene as well as another metal oxide/sulfide combination. However, only a few studies have considered ZnO, Fe, and MXene based composites. Li et al. investigated CO<sub>2</sub> capture and conversion into hydrocarbon fuels (electrochemical reduction) by metal carbides (MXenes) [20]. Geng et al. reported the oxygen vacancies in ZnO nanosheets with an enhanced conversion of CO<sub>2</sub> to CO via electrochemical reduction [21]. Handoko et al. studied the reduction of CO<sub>2</sub> to CH<sub>4</sub> by MXenes (as promising electrocatalysts) [22]. Chitosan-coated Cu<sub>2</sub>O nanoparticles (as a catalyst) used for the electro-reduction of CO<sub>2</sub> to methanol were reported by Basumallick et al. [23]. Hirunsit et al. studied copper based alloys for converting CO<sub>2</sub> to methane and methanol (electrochemical reduction) [24]. Basumallick et al. inspected the electrocatalytic reduction of CO<sub>2</sub> by a ZnO–Cu nanocomposite catalyst [25]. Huan et al. noted the electrochemical reduction of CO<sub>2</sub> to CO using Fe-N-C materials as a catalyst [26]. Based on these studies, in this work, a composite of ZnO, MXene, ZnO-Fe, ZnO-MXene, and ZnO-Fe-MXene was synthesized by a hydrothermal method.

## 2. Results and Discussion

### 2.1. Structural Investigation

The XRD pattern of the ZnO-Fe-MXene nanocomposite (Figure 1a) revealed the formation of a hexagonal well crystallized single-phase material. There were no contamination peaks or secondary phase detected in the XRD pattern of ZnO-Fe-MXene nanocomposite, and the crystallographic planes monitored at (1 0 0), (0 0 2), (1 0 1), and (1 1 0) as per JCPDS No: 65-2908 were indicated as being in ZnO phase. The crystallographic planes observed at (0 0 2), (1 0 3), and (1 0 5) as per JCPDS No: 52-0875 were indicated as being in the MXene phase [12]. Small diffraction peaks beside ZnO (1 0 0) and ZnO (1 0 1) were also detected. These may be from the impurities or residual organic compounds remaining in the product. In this paper, iron was doped in the zinc oxide with MXene, and there were two valence states of iron. In the literature, the iron in zinc oxide is trivalent, and the radii of Fe<sup>3+</sup> (0.078 nm) and Zn<sup>2+</sup> (0.074 nm) are close, so the changes in the lattice constant, crystallite size, dislocation density, and lattice strain are small, and the ZnO material does not undergo significant lattice distortion. Figure 1a shows the XRD pattern of the iron-doped zinc oxide. Compared with that of ZnO (hexagonal), the structure of zinc oxide after Fe doping is a hexagonal structure, and the doping does not change the symmetry of the crystal structure. Pure, Fe doped ZnO nanoparticles showed crystallite sizes of 27.89 and 18.42 nm, as shown in Table 1. The reason for the decrease in the crystallite size is that the Fe atoms do not shift onto the replacement sites, resulting in crystallinity loss within the hexagonal crystal structure and diminishing the crystallite size, which is also responsible for the enlargement of the peaks. The pointed peaks demonstrate the hexagonal crystalline nature of the synthesized hybrids. From the XRD of the hybrids, it is apparent that the peaks are expanded and have lower intensities owing to the occurrence of etched MXene with Fe doped ZnO nanoparticles. All of the foremost peaks of ZnO and MXene are present in all composite materials, and this is a clear confirmation of the efficient creation of the hybrid composites [27].

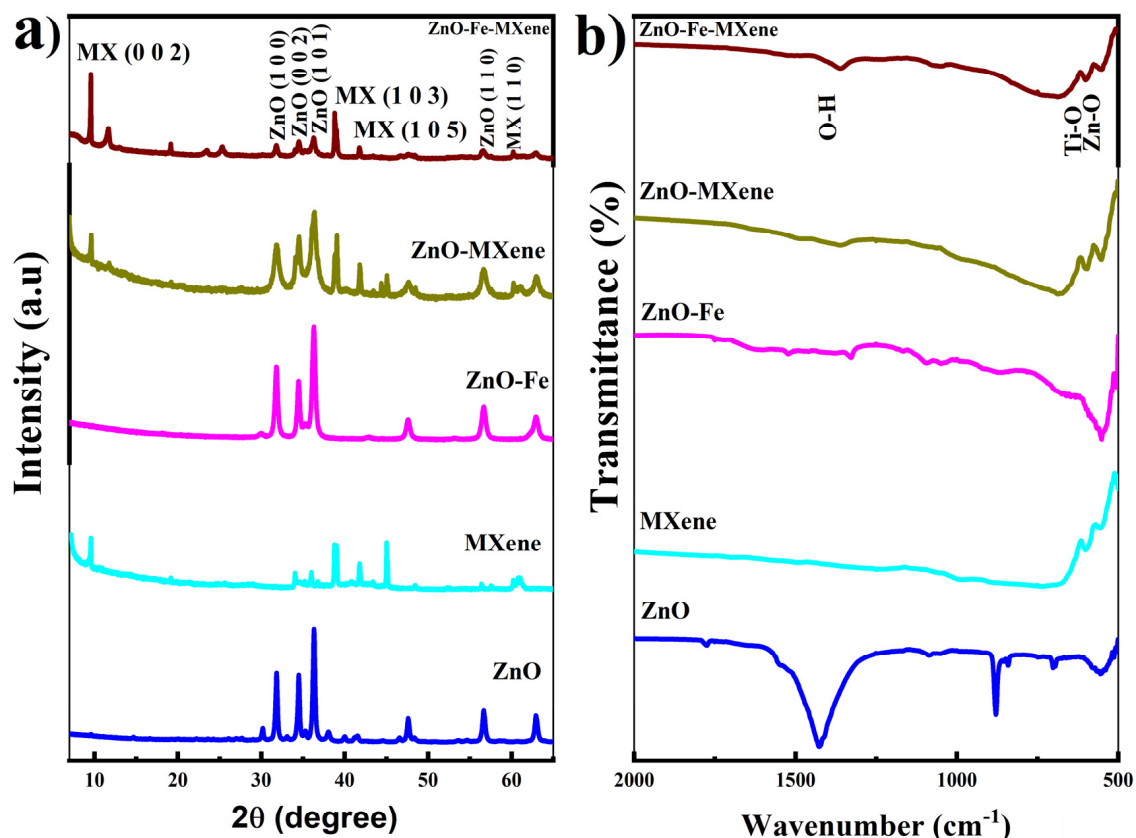


**Figure 1.** (a) XRD pattern; (b) FTIR spectra of the ZnO, MXene, ZnO-Fe, ZnO-MXene, and ZnO-Fe-MXene nanocomposites.

**Table 1.** Lattice parameters obtained from the ZnO, MXene, ZnO-Fe, ZnO-MXene, and ZnO-Fe-MXene nanocomposites.

Sample	Phase	Lattice Constant (nm)	Crystallite Size (nm) $D = k\lambda/\beta \cos\theta$	Dislocation Density ( $\delta$ ) $\times 10^{15}$ (Lines/m <sup>2</sup> ) $\delta = 1/D^2$	Strain ( $\epsilon$ ) $10^{-3}$
ZnO	Hexagonal	a = 0.3231 c = 0.5164	27.89	1.29	1.243
MXene	Hexagonal	a = 0.3072 c = 0.1851	20.57	2.36	1.685
ZnO-Fe	Hexagonal	a = 0.3224 c = 0.5172	18.42	2.95	1.882
ZnO-MXene	ZnO (hexagonal)	a = 0.3220 c = 0.5180	7.9	16.0	4.348
	MXene (hexagonal)	a = 0.3068 c = 0.1853	17.9	3.12	1.931
ZnO-Fe-MXene	ZnO-Fe (hexagonal)	a = 0.3228 c = 0.5160	10.20	9.61	3.398
	MXene (hexagonal)	a = 0.3063 c = 0.1860	24.16	1.71	1.435

## 2.2. FTIR Studies

The FTIR spectrum obtained for the ZnO-Fe-MXene nanocomposite is shown in Figure 1b. The FTIR studies validated the bending and stretching vibrations of saturated hydrocarbons (–CH), hydrogen bonds (–OH), and carbonyls (–CO), respectively. A strong broad peak observed in the range

1362–3443  $\text{cm}^{-1}$  could be due to the bending and stretching vibrations of O–H groups. Carbonyl group ( $\text{CO}_3^{2-}$ ) bending vibration is detected at 1125 and 2922  $\text{cm}^{-1}$ . The Zn–O and Ti–O modes of stretching correspond to peaks at 545–600  $\text{cm}^{-1}$  [28,29].

### 2.3. Morphological Analysis

The SEM photographs obtained for the ZnO-Fe, ZnO-MXene, and ZnO-Fe-MXene nanocomposites are shown in Figure 2a–c. From the micrograph (Figure 2a–c), it is observable that the surface of the hydrothermally prepared ZnO-Fe-MXene nanocomposite is smooth with a flower-like structure. The average grain size of the powder was found to be around 100 nm. The doping of Fe and MXene does appear to have a noteworthy effect on the morphology of ZnO; titanium carbides can be isolated on the surface of ZnO, which might have controlled the growth to minute grains.

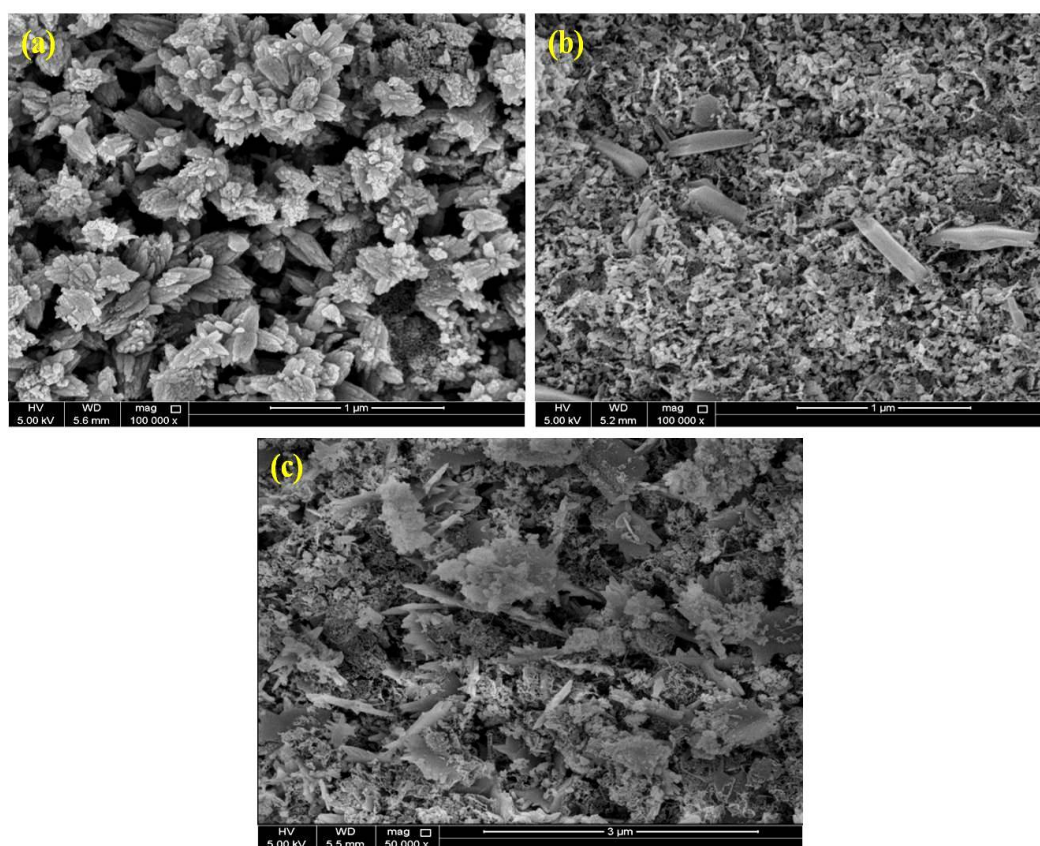


**Figure 2.** SEM images of the (a) ZnO-Fe, (b) ZnO-MXene, and (c) ZnO-Fe-MXene nanocomposites.

The EDAX spectra obtained for the hydrothermally prepared ZnO-Fe, ZnO-MXene, and ZnO-Fe-MXene nanocomposites are shown in Figure 3a–c. The chemical composition data derived for the samples from the EDS analysis (wt %) are indicated as Zn (28.72%), Fe (3.55%), Ti (21.38%), Al (1.65%), C (18.26%), and O (26.44%), as shown in Figure 3. A small amount of TiC was still present, as indicated by the MAX phase and also authenticated by the occurrence of O and a small amount of F, Cl dealing with EDAX results. From the data, it was found that the elements were present as per the requirements, and the EDAX validated the effective incorporation of MXene into the ZnO nanostructure.

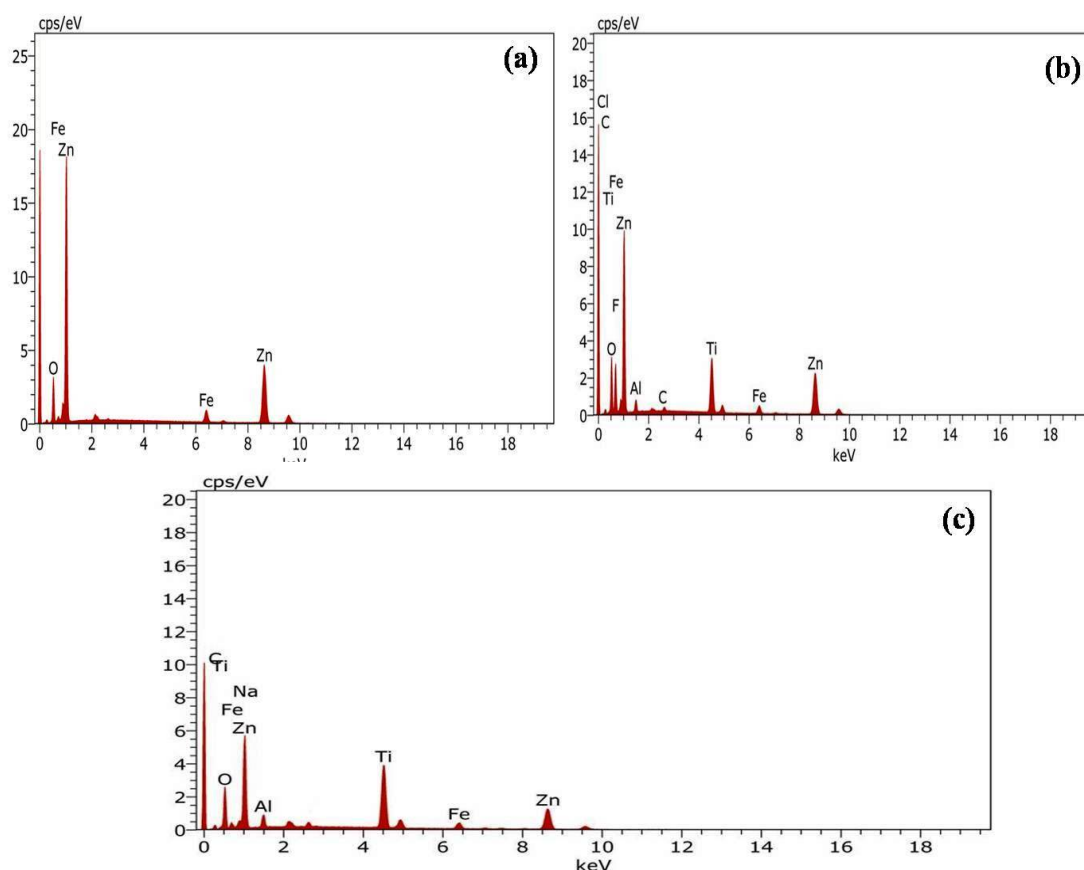


**Figure 3.** EDAX spectrum for the (a) ZnO-Fe, (b) ZnO-MXene, and (c) ZnO-Fe-MXene nanocomposites.

#### 2.4. Electrochemical Properties of the ZnO-Fe-MXene Nanocomposite

To investigate the CO<sub>2</sub> reducing behaviour of the ZnO, MXene, ZnO-Fe, ZnO-MXene, and ZnO-Fe-MXene nanocomposites (Figure S1), CV was conducted in the  $-1.0$  to  $+0.4$  V vs. E (V vs. Ag/AgCl) potential range for ZnO, MXene, ZnO-Fe, ZnO-MXene, and ZnO-Fe-MXene nanocomposite electrodes in N<sub>2</sub> and CO<sub>2</sub> saturated in 0.5M NaOH (Figure 4a). The smaller reduction redox peak at  $-0.99$  V was identified as ambient CO<sub>2</sub> produced from surface reduction. Nevertheless, in the case of ZnO-Fe-MXene, when the electrode was checked in N<sub>2</sub> conditions, no peak was observed. It is interesting to note that when the ZnO-Fe-MXene electrode is analyzed under CO<sub>2</sub> producing circumstances, the current density increases up to  $-18$  mAcm<sup>-2</sup> ( $-1.0$  V), and the onset potential moves in the direction of positive potential ( $-0.04$  V). In comparison to the electrode when checked under N<sub>2</sub> (Figure 4b), the current density is  $-0.02$  mAcm<sup>-2</sup> ( $-1.0$  V) while the onset potential is  $-0.85$  V, proving the improved electrochemical reducing (eCR) activity of ZnO-Fe-MXene electrocatalysts. The difference in the current obtained in presence of N<sub>2</sub> and CO<sub>2</sub> shows that bicarbonate is not participating in the reduction process. Similarly, CV analysis for ZnO, MXene, ZnO-Fe, and ZnO-MXene was also conducted under CO<sub>2</sub> conditions as illustrated in Figure 4. In order to determine whether MXene affected the catalytic activity of the ZnO-Fe catalyst, the CV of the catalyst was executed in a CO<sub>2</sub> saturated 0.1 M NaOH electrolyte and showed a large capacitive current with an increase in the cathodic current to  $-0.7$  V, likely due to either H<sup>+</sup> and/or CO<sub>2</sub> reduction. The results imply that the eCR activity of the ZnO-Fe-MXene nanocomposite based electrode in the direction of CO<sub>2</sub> reduction is very high (Table 2) compared with that found with the pure ZnO, MXene, ZnO-Fe, and ZnO-MXene samples [30–32].



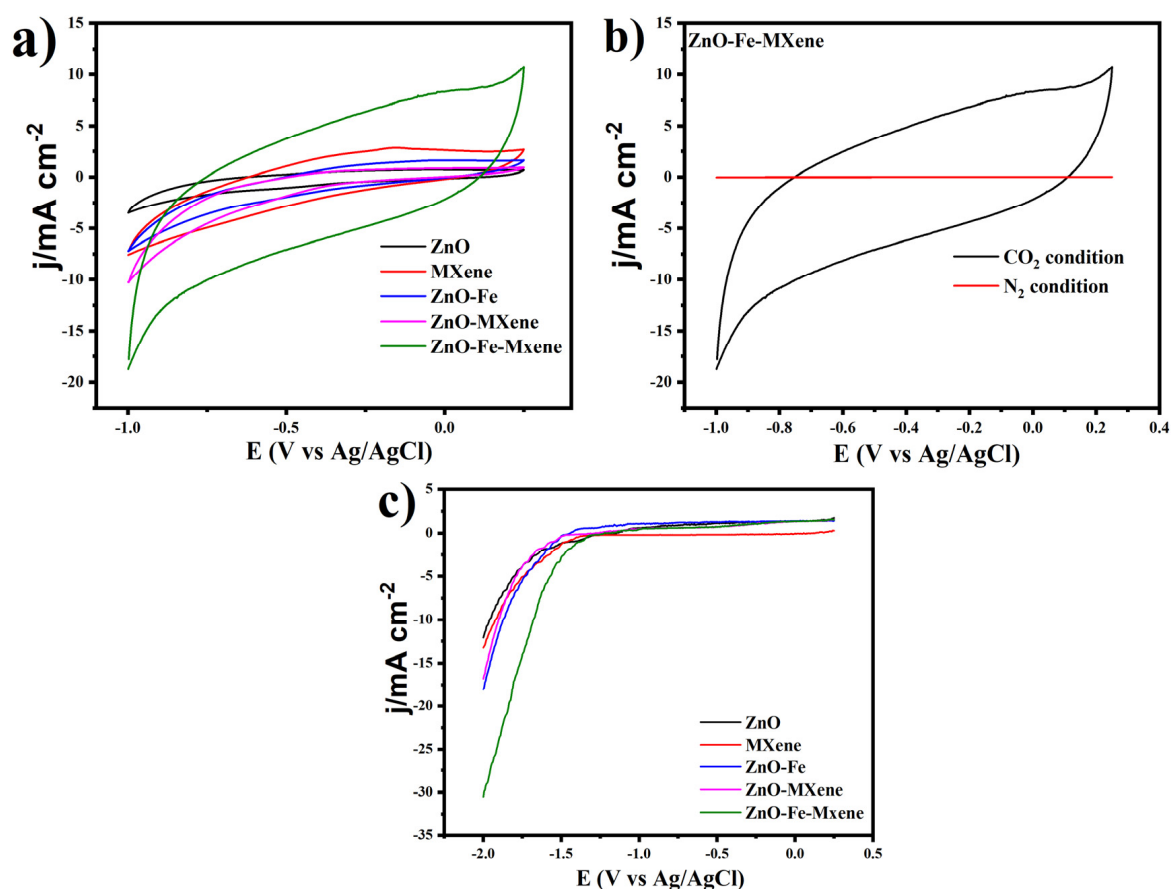


**Figure 4.** Cyclic voltammetry (CV) studies of the (a) ZnO, MXene, ZnO-Fe, ZnO-MXene, and ZnO-Fe-MXene nanocomposites in a CO<sub>2</sub> saturated aqueous solution of 0.5 M NaOH at a scan rate of 50 mV/s; and (b) ZnO-Fe-MXene nanocomposite under CO<sub>2</sub> and N<sub>2</sub> conditions. (c) Linear sweep voltammogram studies of the ZnO, MXene, ZnO-Fe, ZnO-MXene, and ZnO-Fe-MXene nanocomposites at a scan rate of 50 mV/s.

**Table 2.** Current density of prepared nanomaterials at a scan rate of 50 mV/s under CO<sub>2</sub> conditions.

Materials	Current Density (mAcm <sup>-2</sup> )
ZnO	3.439
MXene	6.64
ZnO-Fe	7.13
ZnO-MXene	10.21
ZnO-Fe-MXene	18.745

The LSV showed superior produced reduction currents for the ZnO-Fe-MXene nanocomposite (Figure 4c). Clearly, the total current densities (reaction rates) are significantly increased in the case of the CO<sub>2</sub> saturated electrolyte, indicating a noteworthy role of the CO<sub>2</sub> reduction reaction in the overall reduction processes and, thus, the high activity of the ZnO-Fe-MXene nanocomposite in CO<sub>2</sub> conversion [33–38].

The EIS is one more outstanding method for investigating the CO<sub>2</sub> conversion activity of prepared composites [39]. The potentiostatic mode (three-electrode system) in a 0.5 M NaOH solution with an alternating GCE in the frequency range 0.2–100,000 Hz, a peak potential of 0.46 V, and an amplitude of 10 mV is used for the EIS. In electrochemical studies, two noteworthy factors are the (a) solution resistance and (b) resistance between the working and reference electrodes. The Nyquist plots (Figure 5a,b) of all the prepared composites, illustrating a semicircle impedance curve (high-frequency region), are related

to the discrete frequency, and those in the low-frequency region with a slope of  $45^\circ$  corresponded to a straight line, conveying the Warburg diffusion impedance. The semicircle (high-frequency region) is also related to the partial reduction of methanol to formic acid [40–42]. The charge transfer resistance at the electrode–electrolyte boundary or the chunking properties of the rough electrode responsible for the faradic process of the ionic exchange is represented by the semicircle’s diameter. The small semicircle diameter implies amplified reaction kinetics, and the low charge transfer resistance suggests an astonishing interfacial structural change, which most likely results from the Ti-based framework (high electrical conductivity). Amongst the dissimilar nanocomposites, the ZnO-Fe-MXene composite is the most proficient, which has the lowest resistance to approaching ion and electron transfer, the most movement of reactants toward active sites, a low activation energy, and speedy reaction kinetics [43–47].

The comparison of the EIS spectra of the ZnO, MXene, ZnO-Fe, ZnO-MXene, and ZnO-Fe-MXene nanocomposites demonstrates that the charge transfer resistances in ZnO, MXene, ZnO-Fe, and ZnO-MXene are an order of magnitude higher than that in the ZnO-Fe-MXene nanocomposite in identical conditions. These outcomes show that the conductivity of the composite advances the charge transfer to  $\text{CO}_2$ . Particularly, the charge transfer resistance on ZnO-Fe-MXene is additionally decreased when the electrode is utilized for the eCR reaction. This suggests that the surface of the electrode is not only reducing the  $\text{CO}_2$  throughout the reaction but also stops it from departing during structural reorganization [48,49].

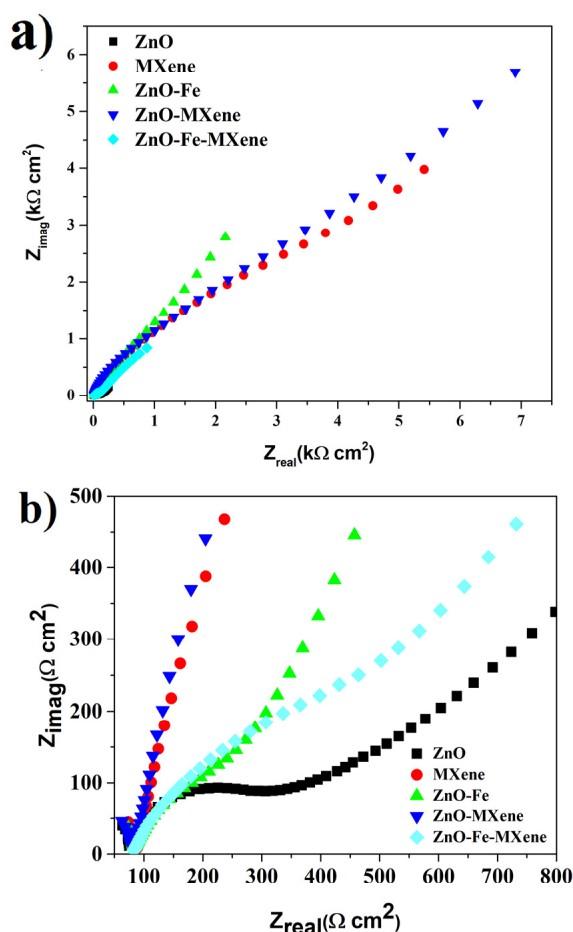


**Figure 5.** (a) Electrochemical impedance spectroscopy (EIS) studies of the various electrodes in the presence of  $\text{CO}_2$  measured in 0.5 M NaOH under an applied potential of 0.2 V at room temperature; (b) Magnified high-frequency region of the prepared composites.

Figure 6 shows the CV analysis for the tested catalysts before and after 1000 cycles of the oxidation test. It can be observed that ZnO-Fe-MXene kept around 88% of its initial CO oxidation current after 1000 cycles, which revealed that it was more stable than ZnO MXene (79%) and MXene (73%). Meanwhile, ZnO and ZnO-Fe gave the lowest stability condition with 66% and 61%, respectively. The superior stability for the ZnO-Fe-MXene nanocomposite is attributed to its inimitable adsorption affinity for CO, which allows the intermediates/products of the reactions to reach oxygenated species, besides the prominent physicochemical merits of MXene, like its high surface area, great conductivity, abundance of active sites, and high electron density. The electrochemical performance of the prepared nanocomposites (catalysts) are compared with previously reported various 2D metal oxides based catalysts (Table 3).

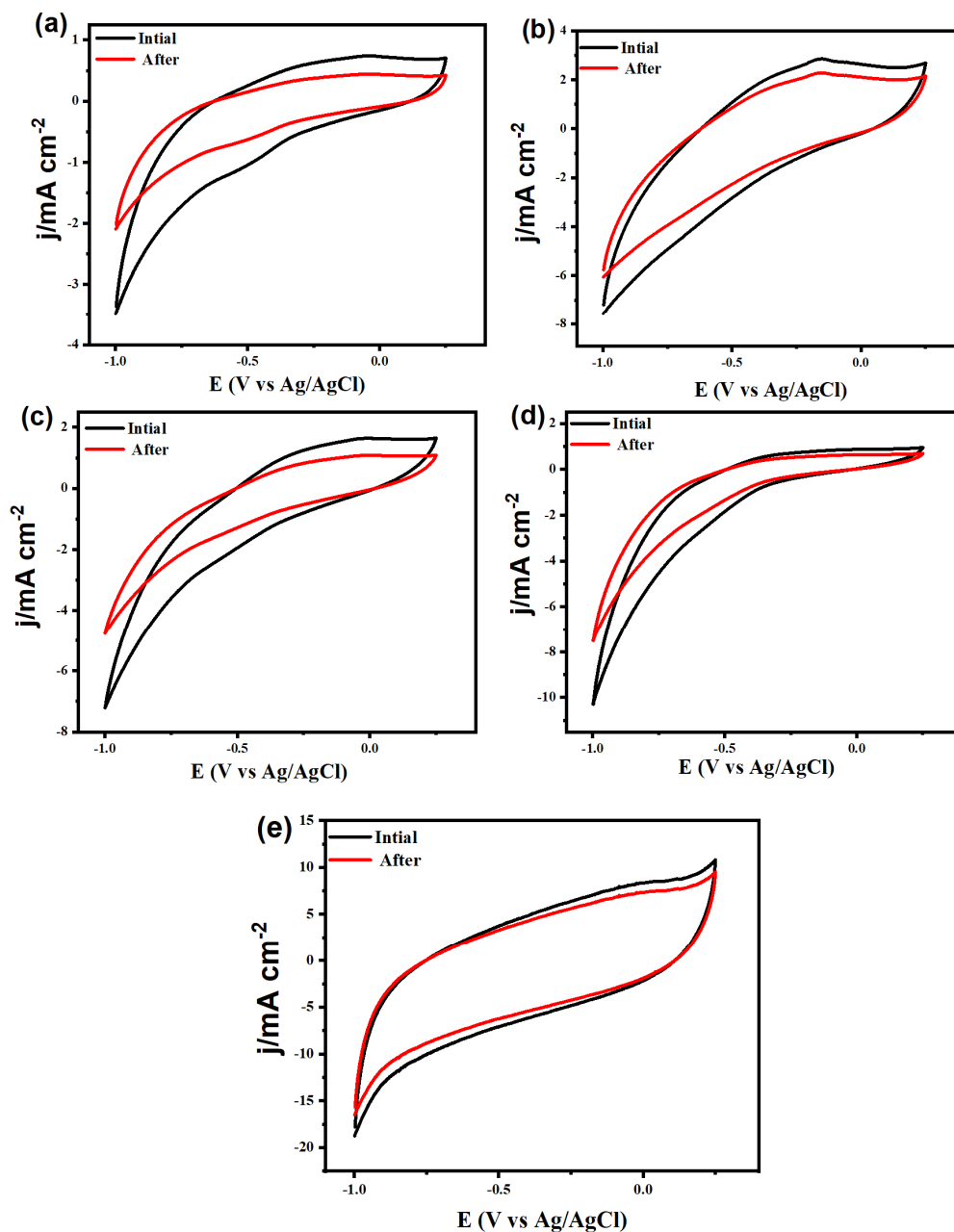


**Figure 6.** The catalyst's stability after 1000 cycles for the (a) ZnO, (b) MXene, (c) ZnO-Fe, (d) ZnO-MXene, and (e) ZnO-Fe-MXene nanocomposites.

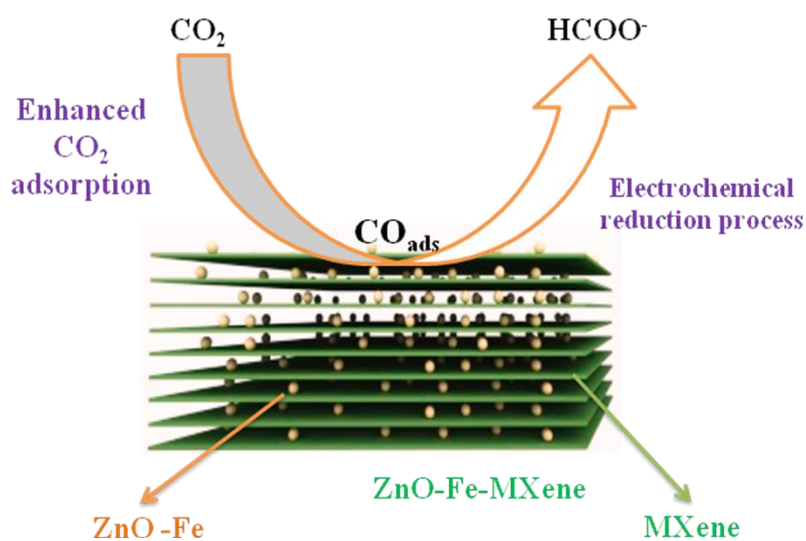


**Table 3.** Comparison of the electrochemical reducing (eCR) performance of various 2D metal oxide based catalysts.

Materials	Method of Preparation	Electrolyte	Current Density (mAcm <sup>-2</sup> )	Ref.
Cu@Sn	In situ electrodeposition	0.5 M NaHCO <sub>3</sub>	16.52	[50]
Cu <sub>x</sub> O-Sn nanowire	Facile surface modification	0.1 M KHCO <sub>3</sub>	4.5	[51]
SnO <sub>2</sub> /graphene	Facile hydrothermal	0.1 M NaHCO <sub>3</sub>	10.2	[52]
SnO <sub>2</sub> /RGO nanosheets	One pot hydrothermal reaction	0.5 M NaHCO <sub>3</sub>	13.9	[53]
AgSn/SnO <sub>x</sub>	Galvanic displacement method	0.5 M NaHCO <sub>3</sub>	16.0	[54]
Cu, S co-doped SnO <sub>2</sub>	Facile hydrothermal	0.5 M NaHCO <sub>3</sub>	5.5	[55]
Zn electrode	Commercial foil	0.1 M KHCO <sub>3</sub>	4.1	[56]
Nanoscale Zn	Anodization	0.5 M NaCl	15.0	[57]
B-doped graphene	Modified hummer's	0.1 M KHCO <sub>3</sub>	2.0	[58]
N-doped graphene	High temperature pyrolysis	0.5 M KHCO <sub>3</sub>	7.5	[59]
g-C <sub>3</sub> N <sub>4</sub> /MWCNTs	Scalable preparation approach	0.1 M KHCO <sub>3</sub>	0.92	[60]
InSn alloy/carbon paper	Electrodeposition	0.1 M KHCO <sub>3</sub>	15.0	[61]
ZnO-Fe-MXene	Hydrothermal route	0.5 M NaOH	18.745	Present study

### 2.5. Comparison of the Electrochemical Reduction Performance of the ZnO, MXene, ZnO-Fe, ZnO-MXene, and ZnO-Fe-MXene Nanocomposite Catalysts

The eCR performances of the ZnO-Fe-MXene hybrids are compared with those of various 2D metal oxide based catalysts. The eCR performance of the ZnO-Fe-MXene hybrid is peculiarly higher than the eCR performance of the ZnO, MXene, ZnO-Fe, and ZnO-MXene electrodes at a variety of functional potentials under similar experimental circumstances. These outcomes suggest that the composite might modify both the geometric and electronic structures of the catalytically active sites. The modification of the ZnO-Fe-MXene catalyst electronic structure is directly communicated to transitional binding (CO- $\%$ ), which can manipulate the pathway reaction for formate creation (Figure 7). In addition, the geometric structure is altered, owing to the fact that oxidation treatment can influence the local atomic distribution at the active site, supporting the stability of CO- $\%$  intermediates [62–64]. Thus, there is a dependable connection between various electronic and morphology effects in ZnO-Fe-MXene electrodes.

**Figure 7.** Reaction mechanism of the eCR on ZnO-Fe-MXene hybrids.

The subsequent structure–property connections from the eCR activity of the composite electrocatalysts:

1. Fe metal suppresses the production of  $H_2$  in favor of  $HCOO^-$  creation, particularly at higher overpotential. This result is magnified when the ZnO-Fe electrodes are utilized for eCR.

2. The result for the ZnO/Fe with MXene composite where ZnO is assisting the enhanced adsorption of  $CO_2$  and reduction activity while Fe is aiding the charge transfer reaction means that the synergy of the electronic and geometric effects is vital for the superior activity of the eCR.

3. The function of MXene is pretty important, and this outcome suggests that a shift in attention would be appropriate, considering the operation of electrocatalysts based on ZnO-Fe for the eCR, where ZnO-Fe can form a composite with MXene similar to 2D materials to achieve better eCR activity. Furthermore, the configuration of  $ZnCO_3$  on the surface of the ZnO-Fe-MXene composite could enhance the mechanism of  $CO_2$  adsorption, which might pave a path towards the enhanced refinement of the eCR electrocatalysts.

4. The superior eCR activity of the ZnO-Fe-MXene electrode relative to that of the ZnO, MXene, ZnO-Fe, and ZnO-MXene electrodes could be attributable to the metal oxide/metal with MXene hybrid structure benefiting from the synergistic electronic and geometric effects of the multi-metallic centers.

### 3. Experimental

#### 3.1. Materials

Zn  $(CH_3COO)_2 \cdot 2H_2O$ , Fe  $(NO_3)_2 \cdot 9H_2O$ ,  $Ti_3AlC_2$ , NaOH, and ethanol were attained from Sigma Aldrich, Germany.

#### 3.2. Preparation of ZnO Nanoparticles

In a distinctive process, 0.22 g of Zn  $(CH_3COO)_2 \cdot 2H_2O$  was dissolved in 20 mL of de-ionized (DI) water and stirred well by using a magnetic stirrer. Then, 1 M of NaOH was mixed with constant stirring for 2 h at 353 K. The mixture was transferred to a 100 mL Teflon-lined stainless-steel autoclave (TLSSA), which was sealed and maintained at 453 K for 12 h. After the reaction, the autoclave was then naturally cooled down to room temperature (RT). The attained precipitate was cleaned off and washed a number of times with DI water and ethanol, correspondingly, and dried at 353 K for approximately 3 h in a hot air oven, before being calcinated in a muffle furnace at 673 K for 2 h.

#### 3.3. Preparation of ZnO-Fe Nanoparticles

In 40 mL of DI water, 0.22 g of Zn  $(CH_3COO)_2 \cdot 2H_2O$  and 0.05 g of Fe  $(NO_3)_2 \cdot 9H_2O$  were dissolved, and the solution was stirred well using a magnetic stirrer. Then, 2 M NaOH was mixed in by constant stirring for 2 h at 353 K. The mixture was transferred to a 100 mL TLSSA, which was sealed and kept at 453 K for 12 h. After the reaction, the TLSSA was then naturally cooled down to RT. The attained precipitate was filtered off and washed a number of times with DI water and ethanol, correspondingly, and dried at 353 K for approximately 3 h in a hot air oven, then calcinated in a muffle furnace at 673 K for 2 h.

#### 3.4. Preparation of ZnO-Mxene Composite

In ethanol, 0.2 g of  $Ti_3C_2$  MXene was dispersed by ultrasonication (20 min) followed by the addition of 0.22 g of Zn  $(CH_3COO)_2 \cdot 2H_2O$  and 2M NaOH into the above solution, and the mixture was stirred well with magnetic stirring for 2 h at 353 K. The mixture was transferred to a 100 mL TLSSA, which was sealed and kept at 453 K for 12 h. After the reaction, the TLSSA was then naturally cooled down to RT. The attained precipitate was filtered off and washed a number of times with DI water and ethanol, correspondingly, and dried at 353 K for approximately 3 h in a hot air oven, then calcinated in a muffle furnace at 673 K for 2 h.

### 3.5. Preparation of the ZnO-Fe-MXene Nanocomposite

In ethanol, 0.2 g of  $\text{Ti}_3\text{C}_2$  MXene was dispersed by ultrasonication (20 min), followed by the addition of 0.22 g of  $\text{Zn}(\text{CH}_3\text{COO})_2 \cdot 2\text{H}_2\text{O}$ , 0.05 g of  $\text{Fe}(\text{NO}_3)_2 \cdot 9\text{H}_2\text{O}$ , and 2M NaOH into the above solution, which was then stirred well with magnetic stirring for 2 h at 353 K. The mixture was transferred to a 100 mL TLSSA, which was sealed and maintained at 453 K for 12 h. After the reaction, the TLSSA was then naturally cooled down to RT. The attained precipitate was filtered off and washed a number of times with DI water and ethanol, correspondingly, and dried at 353 K for approximately 3 h in a hot air oven, then calcinated in a muffle furnace at 673 K for 2 h.

### 3.6. Characterization

An X-ray diffractometer (X'Pert-Pro MPD, PANalytical Co., Almelo, Netherlands) was utilized for the powder XRD analysis of the prepared ZnO, MXene, ZnO-Fe, ZnO-MXene, and ZnO-Fe-MXene nanocomposites. The Fourier transform infrared spectroscopy (FTIR; Perkin Elmer, Frontier, USA FT-IR spectrometer) spectra of the prepared nanocomposites were traced in the range of  $4000\text{--}400\text{ cm}^{-1}$ . The morphological properties of the products were observed with a scanning electron microscope (SEM; Nova Nano SEM 450) equipped with an EDAX (Nova Nano SEM 450).

### 3.7. Electrochemical Reduction of $\text{CO}_2$

Electrochemical experiments were executed with a Gamry electrochemical analyzer (reference 3000, Gamry Co., USA), using a standard 3-electrode system at RT. A platinum wire, Ag/AgCl, and a glassy carbon electrode (GCE) with a diameter of 5 mm were used as counter, reference, and working electrodes, respectively. Two milligrams of prepared nanomaterials (catalyst) were dispersed in a solution, which was a mixture of 200  $\mu\text{L}$  of water and 5  $\mu\text{L}$  of 5% Nafion solution, employing the ultra-sonication technique for one hour to produce black ink with homogeneity. For the sample filling, the GCE was well-polished with 0.05  $\mu\text{m}$  aluminum oxide powder and cleaned meticulously with distilled water. Then, 5  $\mu\text{L}$  of ink was placed on the surface of the GCE and dehydrated beneath an infrared lamp for 10 min to attain a catalyst sheet. For the electrochemical measurements for CO-stripping, the CO was fizzed into a 0.5 M NaOH solution for 15 min. Cyclic voltammetry (CV; reference 3000, Gamry Co., USA) and electrochemical impedance spectroscopy (EIS; reference 3000, Gamry Co., USA) were used. CV was conducted at  $-1.0$  to  $+0.4\text{ V vs. E (V vs. Ag/AgCl)}$  under  $\text{CO}_2$  and  $\text{N}_2$  conditions, with the sweep rate of  $50\text{--}200\text{ mVs}^{-1}$ . ZnO, MXene, ZnO-Fe, ZnO-MXene, and ZnO-Fe-MXene nanocomposite linear sweep voltammetry (LSV) was conducted at  $-2.0$  to  $+0.3\text{ V vs. E (V vs. Ag/AgCl)}$ . EIS data were acquired in a frequency range of  $0.2\text{--}100,000\text{ Hz}$  with amplitude of 10 mV.

## 4. Conclusions

A ZnO-Fe-MXene nanocomposite has been fabricated by the hydrothermal route and was studied for its structural, morphological, and electrochemical properties. XRD verified the ZnO-Fe-MXene (hexagonal, hexagonal) arrangement with an average crystallite size for ZnO-Fe-MXene of 17 nm. Morphological study proved the configuration of the nanoparticles by SEM. The ZnO-Fe-MXene nanocomposite showed the best properties for electron-proton coupling transport during the  $\text{CO}_2$  reduction reaction due to the MXene layer. Finally, a  $\text{CO}_2$  reduction reaction was performed with a hydrothermally prepared ZnO-Fe-MXene nanocomposite. The prepared ZnO-Fe-MXene nanocomposite is a well-organized material that can be employed for performing the oxidation of methanol to formic acid in direct methanol fuel cells. The higher eCR performance of ZnO-Fe-MXene implies that these composites can be utilized industrially and could pave a path toward scalable eCR systems.

**Supplementary Materials:** The following are available online at <http://www.mdpi.com/2073-4344/10/5/549/s1>, Figure S1: CV studies of ZnO, MXene, ZnO-Fe, and ZnO-MXene nanocomposites under  $\text{CO}_2$  and  $\text{N}_2$  conditions.

**Author Contributions:** K.K. and K.K.S. designed the experiment; M.H.S. has their contribution in the electrochemical part and editing in the manuscript; K.K. wrote the original manuscript; K.K.S., B.K., and A.M.A., revise, review, and edit the manuscript. All authors have read and agreed to the published version of the manuscript.

**Funding:** This work was carried by the NPRP grant # NPRP11S-1221-170116 from the Qatar National Research Fund (a member of Qatar Foundation). The statements made herein are solely the responsibility of the authors.

**Acknowledgments:** The authors would like to thank the Central laboratory Unit (CLU), Qatar University, 2713, Doha, Qatar, for SEM with EDAX analysis facility.

**Conflicts of Interest:** The authors declare no conflict of interest.

## References

1. Figueroa, J.D.; Fout, T.; Plasynski, S.; McIlvried, H.; Srivastava, R.D. Advances in CO<sub>2</sub> capture technology—The U.S. Department of Energy’s Carbon Sequestration Program. *Int. J. Greenh. Gas Con.* **2008**, *2*, 9–20. [[CrossRef](#)]
2. Aresta, M.; Dibenedetto, A.A. Angelini Catalysis for the Valorization of Exhaust Carbon: From CO<sub>2</sub> to Chemicals, Materials, and Fuels. Technological Use of CO<sub>2</sub>. *Chem. Rev.* **2014**, *114*, 1709–1742. [[CrossRef](#)] [[PubMed](#)]
3. Qiao, J.; Liu, Y.; Zhang, J. *Electroche Mical Reduction of Carbon Dioxide: Fundamentals and Technologies*, 1st ed.; CRC Press: Boca Raton, FL, USA, 2016.
4. Wu, Z.; Ambrožová, N.; Eftekhari, E.; Aravindakshan, N.; Wang, W.; Wang, Q.; Zhang, S.; Kočí, K.; Li, Q. Photocatalytic H<sub>2</sub> generation from aqueous ammonia solution using TiO<sub>2</sub> nanowires-intercalated reduced graphene oxide composite membrane under low power UV light. *Emergent Mater.* **2019**, *2*, 303–311. [[CrossRef](#)]
5. Wu, J.J.; Zhou, X.D. Catalytic conversion of CO<sub>2</sub> to value added fuels: Current status, challenges, and future directions. *Chin. J. Catal.* **2016**, *37*, 999–1015. [[CrossRef](#)]
6. Zhang, L.; Zhao, Z.J.; Gong, J.L. Nanostructured Materials for Heterogeneous Electrocatalytic CO<sub>2</sub> Reduction and their Related Reaction Mechanisms. *Angew. Chem.* **2017**, *56*, 11326–11353. [[CrossRef](#)]
7. Arán-Ais, R.M.; Gao, D.; Cuenya, B.R. Structure- and Electrolyte-Sensitivity in CO<sub>2</sub> Electroreduction. *Acc. Chem. Res.* **2018**, *51*, 2906–2917. [[CrossRef](#)]
8. Zhang, W.; Hu, Y.; Ma, L.; Zhu, G.; Wang, Y.; Xue, X.; Chen, R.; Yang, S.; Jin, Z. Progress and Perspective of Electrocatalytic CO<sub>2</sub> Reduction for Renewable Carbonaceous Fuels and Chemicals. *Adv. Sci.* **2018**, *5*, 17000275. [[CrossRef](#)]
9. Kannan, K.; Sadasivuni, K.K.; Abdullah, A.M.; Kumar, B. Current Trends in MXene-Based Nanomaterials for Energy Storage and Conversion System: A Mini Review. *Catalysts* **2020**, *10*, 495. [[CrossRef](#)]
10. Feng, D.M.; Sun, Y.; Liu, Z.Q.; Zhu, Y.P.; Ma, T.Y. Designing nanostructured metal-based CO<sub>2</sub> reduction electrocatalysts. *J. Nanosci. Nanotechnol.* **2019**, *19*, 3079–3096. [[CrossRef](#)]
11. Thomas, D.; Augustine, S.; Sadasivuni, K.K.; Ponnamma, D.; Alhaddad, A.Y.; Cabibihan, J.J.; Vijayalakshmi, K.A. Microtron irradiation induced tuning of band gap and photoresponse of Al-ZnO thin films synthesized by mSILAR. *J. Electron. Mater.* **2016**, *45*, 4847–4853. [[CrossRef](#)]
12. Li, K.; Jiao, T.; Xing, R.; Zou, G.; Zhao, Q.; Zhou, J.; Zhang, L.; Peng, Q. Fabrication of hierarchical MXene-based AuNPs-containing core-shell nanocomposites for high efficient catalysts. *Green Energy Environ.* **2018**, *3*, 147–155. [[CrossRef](#)]
13. Thomas, D.; Thomas, A.; Tom, A.E.; Sadasivuni, K.K.; Ponnamma, D.; Goutham, S.; Cabibihan, J.J.; Rao, K.V. Highly selective gas sensors from photo-activated ZnO/PANI thin films synthesized by mSILAR. *Synth. Met.* **2017**, *232*, 123–130. [[CrossRef](#)]
14. Pradeeswari, K.; Venkatesan, A.; Pandi, P.; Karthik, K.; Krishna, K.V.H.; Kumar, R.M. Study on the electrochemical performance of ZnO nanoparticles synthesized via non-aqueous sol-gel route for supercapacitor applications. *Mater. Res. Express* **2019**, *6*, 105525. [[CrossRef](#)]
15. Thomas, D.; Sadasivuni, K.K.; Waseem, S.; Kumar, B.; Cabibihan, J.J. Synthesis, green emission and photosensitivity of Al-doped ZnO film. *Microsyst. Technol.* **2018**, *24*, 3069–3073. [[CrossRef](#)]
16. Thomas, D.; Vijayalakshmi, K.A.; Sadasivuni, K.K.; Thomas, A.; Ponnamma, D.; Cabibihan, J.J. A fast responsive ultraviolet sensor from mSILAR-processed Sn-ZnO. *J. Electron. Mater.* **2017**, *46*, 6480–6487. [[CrossRef](#)]
17. Hezam, A.; Namratha, K.; Drmosh, Q.A.; Chandrashekar, B.N.; Sadasivuni, K.K.; Yamani, Z.H.; Cheng, C.; Byrappa, K. Heterogeneous growth mechanism of ZnO nanostructures and the effects of their morphology on optical and photocatalytic properties. *Cryst. Eng. Comm.* **2017**, *19*, 3299–3312. [[CrossRef](#)]

18. Rosas-Laverde, N.M.; Pruna, A.; Busquets-Mataix, D.; Pullini, D. Graphene Oxide-Assisted Morphology and Structure of Electrodeposited ZnO Nanostructures. *Materials* **2020**, *13*, 365. [[CrossRef](#)]
19. Karthik, K.; Dhanuskodi, S. Synthesis and characterization of ZnO nanoparticles by microwave assisted method. *Intl. J. Emerg. Technol. Innov. Res.* **2018**, *5*, 1022.
20. Hussein Abdullah Alshamarti, A.H. Omran, A. Enhancement characterization of the MSM detector based on Mn doped-ZnO NRS synthesized by microwave assisted chemical bath deposition. *Mater. Sci. Semicond. Process.* **2020**, *114*, 105068. [[CrossRef](#)]
21. Li, N.; Chen, X.; Ong, W.J.; MacFarlane, D.R.; Zhao, X.; Cheetham, A.K.; Sun, C. Understanding of Electrochemical Mechanisms for CO<sub>2</sub> Capture and Conversion into hydrocarbon Fuels in Transition-Metal Carbides (MXenes). *ACS Nano* **2017**, *11*, 10825–10833. [[CrossRef](#)]
22. Geng, Z.; Kong, X.; Chen, W.; Su, H.; Liu, Y.; Cai, F.; Wang, G.; Zeng, J. Oxygen Vacancies in ZnO Nanosheets Enhance CO<sub>2</sub> Electrochemical Reduction to CO. *Angew. Chem. Int. Ed.* **2018**, *57*, 6054–6059. [[CrossRef](#)] [[PubMed](#)]
23. Handoko, A.D.; Khoo, K.H.; Tan, T.L.; Jin, H.; Seh, Z.W. Establishing New Scaling Relations on Two-Dimensional MXenes for CO<sub>2</sub> Electroreduction. *J. Mater. Chem. A* **2018**, *6*, 21885–21890. [[CrossRef](#)]
24. Basumallick, S.; Santra, S. Chitosan coated copper-oxide nanoparticles: A novel electro-catalyst for CO<sub>2</sub> reduction. *RSC Adv.* **2014**, *4*, 63685–63690. [[CrossRef](#)]
25. Hirunsit, P.; Soodsawang, W.; Limtrakul, J. CO<sub>2</sub> electrochemical reduction to methane and methanol on copper-based alloys: Theoretical insight. *J. Phys. Chem. C* **2015**, *119*, 8238–8249. [[CrossRef](#)]
26. Basumallick, S. Electro-reduction of CO<sub>2</sub> onto ZnO–Cu nano composite catalyst. *Appl. Nanosci.* **2020**, *10*, 159–163. [[CrossRef](#)]
27. Huan, T.N.; Ranjbar, N.; Rouse, G.; Sougrati, M.; Zitolo, A.; Mougel, V.; Jaouen, F.; Fontecave, M. Electrochemical Reduction of CO<sub>2</sub> Catalyzed by Fe-N-C Materials: A Structure–Selectivity Study. *ACS Catal.* **2017**, *7*, 1520–1525. [[CrossRef](#)]
28. Karthik, K.; Pushpa, S.; Madhukara Naik, M.; Vinuth, M. Influence of Sn and Mn on structural, optical and magnetic properties of spray pyrolysed CdS thin films. *Mater. Res. Innov.* **2020**, *24*, 82–86. [[CrossRef](#)]
29. Li, Y.; Zhou, X.; Wang, J.; Deng, Q.; Li, M.; Du, S. Young-Hwan Han, Jaehyung Lee, Qing Huang, Facile preparation of in situ coated T<sub>13</sub>C<sub>2</sub>T<sub>x</sub>/N<sub>10.5</sub>Zn<sub>0.5</sub>Fe<sub>2</sub>O<sub>4</sub> composites and their electromagnetic performance. *RSC Adv.* **2017**, *7*, 24698. [[CrossRef](#)]
30. Kottogodaa, I.R.M.; Idris, N.H.; Lu, L.; Wang, J.Z.; Liu, H.K. Synthesis and characterization of graphene–nickel oxide nanostructures for fast charge–Discharge application. *Electrochem. Acta* **2011**, *56*, 5815–5822. [[CrossRef](#)]
31. Ávila-Bolívar, B.; García-Cruz, L.; Montiel, V.; Solla-Gullón, J. Electrochemical Reduction of CO<sub>2</sub> to Formate on Easily Prepared Carbon-Supported Bi Nanoparticles. *Molecules* **2019**, *24*, 2032. [[CrossRef](#)]
32. Choi, J.; Kim, J.; Wagner, P.; Gambhir, S.; Jalili, R.; Byun, S.; Sayyar, S.; Lee, Y.M.; MacFarlane, D.R.; Wallace, G.G.; et al. Energy Efficient Electrochemical Reduction of CO<sub>2</sub> to CO Using a Three-dimensional Porphyrin/Graphene Hydrogel. *Energy Environ. Sci.* **2019**, *12*, 747–755. [[CrossRef](#)]
33. Devi, P.; Malik, K.; Arora, E.; Bhattacharya, S.; Kalendra, V.; Lakshmi, K.V.; Anil, V.; Singh, J.P. Selective Electrochemical Reduction of CO<sub>2</sub> to CO on CuO/In<sub>2</sub>O<sub>3</sub> Nanocomposite: Role of Oxygen Vacancies. *Catal. Sci. Technol.* **2019**, *9*, 5339–5349. [[CrossRef](#)]
34. Parwaiz, S.; Bhunia, K.; Das, A.K.; Khan, M.M.; Pradhan, D. Cobalt-doped ceria/reduced graphene oxide nanocomposite as an efficient oxygen reduction reaction catalyst and supercapacitor material. *J. Phys. Chem. C* **2017**, *121*, 20165–20176. [[CrossRef](#)]
35. Huang, T.; Mao, S.; Zhou, G.; Zhang, Z.; Wen, Z.; Huang, X.; Ci, S.; Chen, J. A high-performance catalyst support for methanol oxidation with graphene and vanadium carbonitride. *Nanoscale* **2015**, *7*, 1301–1307. [[CrossRef](#)]
36. Yu, E.H.; Scott, K.; Reeve, R.W. A study of the anodic oxidation of methanol on Pt in alkaline solutions. *J. Electroanal. Chem.* **2003**, *547*, 17–24. [[CrossRef](#)]
37. Niu, L.; Li, Q.; Wei, F.; Chen, X.; Wang, H. Electrochemical impedance and morphological characterization of platinum-modified polyaniline film electrodes and their electrocatalytic activity for methanol oxidation. *J. Electroanal. Chem.* **2003**, *544*, 121–128. [[CrossRef](#)]
38. Zhu, X.; Zhang, P.; Xu, S.; Yan, X.; Xue, Q. Free-standing three-dimensional graphene/manganese oxide hybrids as binder-free electrode materials for energy storage applications. *ACS Appl. Mater. Interfaces* **2014**, *6*, 11665–11674. [[CrossRef](#)]



39. Hussain, Z.; Ojha, R.; Martin, L.L.; Bond, A.M.; Ramanathan, R.; Bansal, V. Controlling the morphological and redox properties of the CuTCNQ catalyst through solvent engineering. *Emergent Mater.* **2019**, *2*, 35–44. [[CrossRef](#)]
40. Ren, X.; Lu, Q.; Liu, L.; Liu, B.; Wang, Y.; Liu, A.; Wu, G. Current progress of Pt and Pt– based electrocatalysts used for fuel cells. *Sustain. Energy Fuels* **2020**, *4*, 15–30. [[CrossRef](#)]
41. Murata, T.; Kotsuki, K.; Murayama, H.; Tsuji, R.; Morita, Y. Metal-free electrocatalysts for oxygen reduction reaction based on trioxotriangulene. *Commun. Chem.* **2019**, *2*, 46. [[CrossRef](#)]
42. Ma, R.; Lin, G.; Zhou, Y.; Liu, Q.; Zhang, T.; Shan, G.; Yang, M.; Wang, J. A review of oxygen reduction mechanisms for metal-free carbon-based electrocatalysts. *NPJ Comput. Mater.* **2019**, *5*, 78. [[CrossRef](#)]
43. Zhou, S.; Yang, X.; Pei, W.; Liu, N.; Zhao, J. Heterostructures of MXene and N-doped graphene as highly active bifunctional electrocatalysts. *Nanoscale* **2020**, *14*, 10876–10883. [[CrossRef](#)] [[PubMed](#)]
44. Hong, S.; Rhee, C.K.; Sohn, Y. Photoelectrochemical hydrogen evolution and CO<sub>2</sub> reduction over MoS<sub>2</sub>/Si and MoSe<sub>2</sub>/Si nanostructures by combined photoelectrochemical deposition and rapid thermal annealing process. *Catalysis* **2019**, *9*, 494. [[CrossRef](#)]
45. Wang, Y.; Niu, C.; Zhu, Y. Copper–Silver Bimetallic Nanowire Arrays for Electrochemical Reduction of Carbon Dioxide. *Nanomaterials* **2019**, *9*, 173. [[CrossRef](#)] [[PubMed](#)]
46. Li, H.; Zhang, W.; Liu, D.; Li, W. Template-directed synthesis of mesoporous TiO<sub>2</sub> materials for energy conversion and storage. *Emergent Mater.* **2020**. [[CrossRef](#)]
47. Shah, S.; Shah, M.; Shah, A. Evolution in the membrane-based materials and comprehensive review on carbon capture and storage in industries. *Emergent Mater.* **2020**, *3*, 33–44. [[CrossRef](#)]
48. Zhang, S.; Zhuo, H.; Li, S.; Bao, Z.; Deng, S.; Zhuang, G.; Zhong, X.; Wei, Z.Z.; Yao, Z.; Wang, J. Effects of surface functionalization of MXene based nanocrystals on hydrogen evolution reaction performance. *Catal. Today* **2020**. [[CrossRef](#)]
49. He, J.; Johnson, N.J.J.; Huang, A.; Berlinguette, C.P. Electrocatalytic alloys for CO<sub>2</sub> reduction. *Chem. Sustain. Chem.* **2018**, *11*, 48–57. [[CrossRef](#)]
50. Childers, D. *An Exploration of Geometric and Electronic Effects in Metal Nanoparticles Catalysts*; Chemical Engineering, University of Illinois: Chicago, IL, USA, 2014.
51. Hou, X.; Cai, Y.; Zhang, D.; Li, L.; Zhang, X.; Zhu, Z.; Peng, L.; Liu, Y.; Qiao, J. 3D core shell porous-structured Cu@Sn hybrid electrodes with unprecedented selective CO<sub>2</sub>– into-formate electroreduction achieving 100%. *J. Mater. Chem. A* **2019**, *7*, 3197–3205. [[CrossRef](#)]
52. Zhao, Y.; Wang, C.; Wallace, G.G. Tin nanoparticles decorated copper oxide nanowires for selective electrochemical reduction of aqueous CO<sub>2</sub> to CO. *J. Mater. Chem. A* **2016**, *4*, 10710–10718. [[CrossRef](#)]
53. Zhang, S.; Kang, P.; Meyer, T.J. Nanostructured tin catalysts for selective electrochemical reduction of carbon dioxide to formate. *J. Am. Chem. Soc.* **2014**, *136*, 1734–1737. [[CrossRef](#)] [[PubMed](#)]
54. Li, F.; Chen, L.; Xue, M.; Williams, T.; Zhang, Y.; MacFarlane, D.R.; Zhang, J. Towards a better Sn: Efficient electrocatalytic reduction of CO<sub>2</sub> to formate by Sn/SnS<sub>2</sub> derived from SnS<sub>2</sub> nanosheets. *Nano Energy* **2017**, *31*, 270–277. [[CrossRef](#)]
55. Luc, W.; Collins, C.; Wang, S.; Xin, H.; He, K.; Kang, Y.; Jiao, F. Ag–Sn bimetallic catalyst with a core-shell structure for CO<sub>2</sub> reduction. *J. Am. Chem. Soc.* **2017**, *139*, 1885–1893. [[CrossRef](#)] [[PubMed](#)]
56. Hu, X.; Yang, H.; Guo, M.; Gao, M.; Zhang, E.; Tian, H.; Liang, Z.; Liu, X. Synthesis and characterization of (Cu, S) Co-doped SnO<sub>2</sub> for electrocatalytic reduction of CO<sub>2</sub> to formate at low overpotential. *Chem. Electron. Chem.* **2018**, *5*, 1330–1335. [[CrossRef](#)]
57. Kuhl, K.P.; Hatsukade, T.; Cave, E.R.; Abram, D.N.; Kibsgaard, J.; Jaramillo, T.F. Electrocatalytic Conversion of Carbon Dioxide to Methane and Methanol on Transition Metal Surfaces. *J. Am. Chem. Soc.* **2014**, *136*, 14107–14113. [[CrossRef](#)]
58. Quan, F.; Zhong, D.; Song, H.; Jia, F.; Zhang, L. A highly efficient zinc catalyst for selective electroreduction of carbon dioxide in aqueous NaCl solution. *J. Mater. Chem. A* **2015**, *3*, 16409–16413. [[CrossRef](#)]
59. Sreekanth, N.; Nazrulla, M.A.; Vineesh, T.V.; Sailaja, K.; Phani, K.L. Metal-free boron-doped graphene for selective electroreduction of carbon dioxide to formic acid/formate. *Chem. Commun.* **2015**, *51*, 16061–16064. [[CrossRef](#)]
60. Wang, H.X.; Chen, Y.B.; Hou, X.L.; Ma, C.Y.; Tan, T.W. Nitrogen-doped graphenes as efficient electrocatalysts for the selective reduction of carbon dioxide to formate in aqueous solution. *Green. Chem.* **2016**, *18*, 3250–3256. [[CrossRef](#)]



61. Lu, X.Y.; Tan, T.H.; Ng, Y.H.; Amal, R. Highly selective and stable reduction of CO<sub>2</sub> to CO by a graphitic carbon nitride/carbon nanotube composite electrocatalyst. *Chem. Eur. J.* **2016**, *22*, 11991–11996. [[CrossRef](#)]
62. Lai, Q.; Yang, N.; Yuan, G. Highly efficient In–Sn alloy catalysts for electrochemical reduction of CO<sub>2</sub> to formate. *Electrochem. Commun.* **2017**, *83*, 24–27. [[CrossRef](#)]
63. He, J.; Dettelbach, K.E.; Huang, A.; Berlinguette, C.P. Berlinguette, Brass and Bronze as Effective CO<sub>2</sub> Reduction Electrocatalysts. *Angew. Chem. Int. Ed.* **2017**, *56*, 16579–16582.
64. Rasul, S.; Pugniant, A.; Xiang, H.; Eileen, J.M.F.; Yu, H. Low cost and efficient alloy electrocatalysts for CO<sub>2</sub> reduction to formate. *J. CO<sub>2</sub> Util.* **2019**, *32*, 1–10. [[CrossRef](#)]



© 2020 by the authors. Licensee MDPI, Basel, Switzerland. This article is an open access article distributed under the terms and conditions of the Creative Commons Attribution (CC BY) license (<http://creativecommons.org/licenses/by/4.0/>).